

A non-Linear Model suitable for the Off-line co-Simulation of Fault-tolerant PM Motors

M. Tursini, M. Villani, A. Di Tullio, G. Fabri and F. Parasiliti Collazzo

Abstract -- This paper presents a dynamic model suitable for accurate co-simulation of fault-tolerant permanent-magnet motor drives featuring independent-phases structure. The model is developed in a circuital form where the usual inductive parameters and back-EMF coefficient are replaced by current and rotor position dependent functions, so that the exact electromagnetic nature and geometry of the machine is accounted over the large flux-current operating range.

The model functions are pre-computed by a finite element method analysis of a single phase of the machine, once the magnetic independence among the phases has been verified. Then, the circuital model is solved by a dynamical simulator which implements also the drive system, converter and control, following on the off-line co-simulation approach.

The proposed model is validated by experiments carried on a fault-tolerant five-phase permanent-magnet motor-drive for aeronautical application, controlled by BLDC technique.

The results show that the modeling solution is capable to simulate the motor dynamics with a high degree of accuracy, and can be used for an effective rapid prototyping of fault-tolerant drives.

Index Terms--Modeling, simulation, multiphase machines, fault-tolerant machines, finite element analysis, BLDC drives, virtual prototyping.

I. INTRODUCTION

THE use of dynamic simulation tools to predict the performance of electrical drives is widely practiced from about twenty years [1].

These tools basically make available “linear” models of the electrical machine, i.e. the machine is modeled by a set of (non linear) differential equations with constant coefficients, where the electromagnetic nature is accounted by constant parameters, i.e. the flux-current relation is assumed “linear”. The time solution of such models is implementable by a wide choice of solver algorithms (fixed or variable step) and the dynamic tools also allow for the simulation of the other relevant drive subsystems such as power converter and control stages. The overall computation is very fast still by using standard computers and permits to obtain a good basic description of the drive behavior, [2].

Custom arrangements of the models are possible by variable coefficients or functions when one must consider non-linear flux-current or flux-position relationships. In these cases a greater deepening of the nature of the machine is needed, either by experimental testing (on an existing machine) or by a Finite Element Method (FEM) analysis

Marco Tursini, Marco Villani, Alessio Di Tullio, Giuseppe Fabri and Francesco Parasiliti Collazzo are with the Department of Electrical and Information Engineering, University of L’Aquila, I-67100, L’Aquila, Italy.

(usually at prototyping), [3][4][5].

To increase the accuracy of the motor modeling of a drive system, a “co-simulation” approach can be used, [6][7].

By this method, the electrical machine is simulated by a tool for FEM analysis of electromagnetic fields, while the drive system (power converter and control) is implemented by a simulator of dynamic systems, [8][9]. Such integration of software tools ensures high accuracy in simulation, which is a key goal during virtual prototyping. Unfortunately, it requires large amount of hardware resources and computation times, as the (heavy) FEM computation is carried out at each time step and this must be sufficiently small to comply with the dynamics of the overall drive system, [10][11].

Thereafter, an “off-line” implementation of the co-simulation technique has been also proposed, Fig. 1.

In this case all the drive subsystems are processed by the dynamic simulator at run-time, but the (electrical) model of the machine is implemented so that it complies with pre-computed electromagnetic (static) analyses of a FEM model, [12]. The off-line analysis must span over the whole (realistically possible) operative range of the phase currents and rotation period, in order to produce a “mapping” of the model functions. But, once this activity has been completed, all the following dynamic studies will be free of the high computation charge of the FEM computation.

The same (and in some case greater) level of accuracy of the co-simulation is achieved, but with a strong reduction of the overall computation times. For these advantages most of the FEM software packages allows for the generation of maps usable for co-simulation, but not for custom or new machine topologies, [13][14].

A particular interest on these issues can be seen in the virtual prototyping of the fault tolerant machines, [15][16][17].

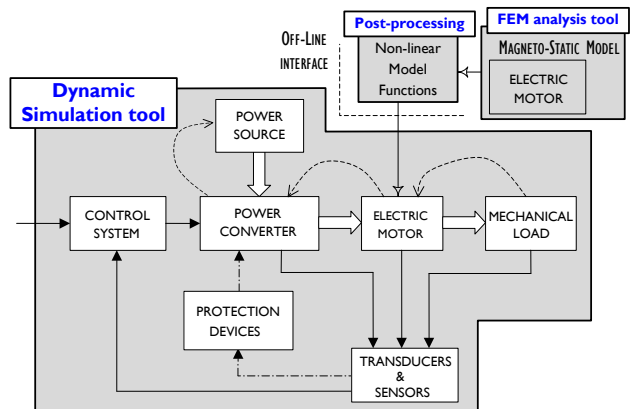


Fig. 1. Off-line co-simulation of electrical drives.

These are multiphase machines designed to possess full independence between the phases from the electrical, magnetic, and thermal points of view. In the “open-phase” faulty modes, the opening of one or more faulted phases forces the healthy ones to increase their current and saturate the respective magnetic paths to maintain the same load conditions, [18][19]. As a consequence, also the dynamic response of the controlled machine is modified, the reason for which a more accurate model is necessary for a realistic performance prediction.

In this paper a dynamic non-linear model suitable for accurate co-simulation of fault-tolerant Permanent Magnet (PM) motors with independent-phases structure is presented, [20]. The model is arranged in a circuital form where the usual inductive parameters and back-EMF coefficient are replaced by current and rotor position dependent functions, so that the large flux-current operating range of fault-tolerant machines is covered. Based on the off-line co-simulation approach, the model functions are pre-computed by a FEM analysis of a single phase of the machine, once the magnetic independence among the phases has been verified. Then, the non-linear model is solved by a dynamical simulator which implements both the machine and the drive system (converter and control). The proposed model is validated by experiments carried on a fault-tolerant five-phase PM motor-drive for aeronautical application, controlled by BLDC technique.

The plan of the paper is as follows: at beginning, the distinctive features of the fault-tolerant PM motor drive are recalled in Section II, the proposed circuital model is presented in Section III, the drive scheme and the simulation model are described in Section IV; then the experimental validation is reported in Section V, and, finally, conclusions are given in Section VI.

II. FAULT-TOLERANT PM MOTOR DRIVE

The electric machine considered in this paper is a 5-phase, 18 poles, 20 slots, PM motor designed to fulfil the requirements of an avionic flap-actuator, [21]. Due to the safety critical application, degraded operating modes are specified in case of the lack of one or two phases, Table I.

The motor structure is shown in Fig. 2. It is based on the principle of electrical, magnetic, and thermal independence between the phases which is the key feature in fault-tolerant machines.

TABLE I:
SPECIFICATIONS OF THE ELECTRIC MOTOR FOR FLAP ACTUATOR

DC voltage supply (max)	[V]	250
Rated torque	[Nm]	12.0 @ 600 rpm
Starting torque	[Nm]	21.0 @ 150 rpm
Torque with 1 phase open	[Nm]	12.0 @ 600 rpm
Torque with 2 phase open	[Nm]	12.0 @ 400 rpm
Weight	[kg]	< 3.5
Working Duty Cycle	[%]	5

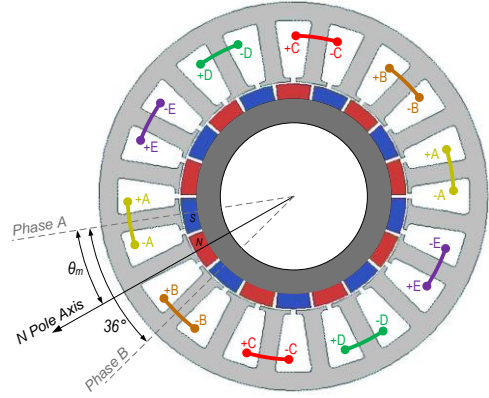


Fig. 2. Structure and windings arrangement of the 5-phase PM motor.

Each phase consists of two series coils located on opposite poles. The coils of one phase are wound on a single tooth (concentrate windings), so as to eliminate overlapping of conductors of different phases in the heads: this feature prevents phase-to-phase short circuits, more critical than those related to a single phase. Each stator slot contains conductors of a single phase (“alternate” teeth windings): this expedient maximizes the thermal insulation and minimizes the mutual magnetic coupling between the phases, [22][23].

The motor is designed to comply for the degraded modes specifications according to the thermal limits and the service involved. The results of the FEM design are summarized in Table II, which shows how in the worst case (two phases open) the amplitude of the BLDC current increases about three fold respect to the rated one.

TABLE II:
RESULTS OF THE FEM DESIGN

Operating conditions	Current [A]	Average torque [Nm]	Service
Rated	5	12.6	continuous
Start-up	11	21.4	limited
One phase open	7	13.0	limited
Two phases open	14	12.9	Strongly limited

III. MOTOR MODELING

Detailed FEM analyses and experimental tests have proven that the operation of such kind of fault-tolerant motor can be represented, with great accuracy, by the straightforward superposition of the effects of each single phase assumed to operate alone (“one-phase feeding”). These results confirm the magnetic independence between the motor phases and permits to circumscribe to a single phase the dynamic modeling and the FEM analysis needed to evaluate the model functions. The aspects related to these assumptions are discussed in the following.

A. One-phase feeding

The proposed model is based on the computation of the flux linkage and electromagnetic torque as functions of the phase current and rotor position. These behaviors are shown in Fig. 3 and Fig. 4; they are computed over the whole period of the electrical angle and current values ranging up to extreme fault-tolerant operating conditions. The effects of

flux saturation at high currents are clearly visible, such as the torque asymmetries due to the geometry of the machine.

Fig. 5 and Fig. 6 show the typical flux line distribution computed by the FEM model when only the phase A is fed, while the rotor position is such that one north pole of the rotor magnets is respectively aligned or in quadrature with the axis of the fed coil. The trace of the cross section used to compute the coil flux linkage is also shown, drawn over one of the two opposite wound teeth of the phase.

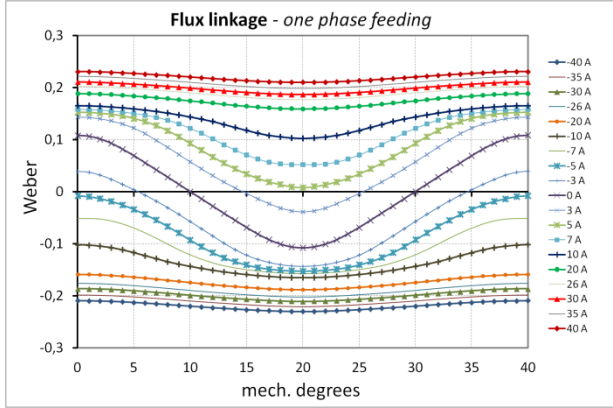


Fig. 3. Flux linkage vs. rotor angle for different current levels (feeding of phase A , static FEM analysis).

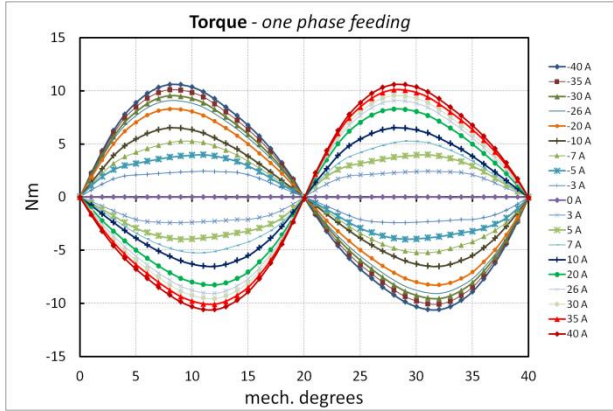


Fig. 4. Torque vs. rotor angle for different current levels, (feeding of phase A , static FEM analysis).

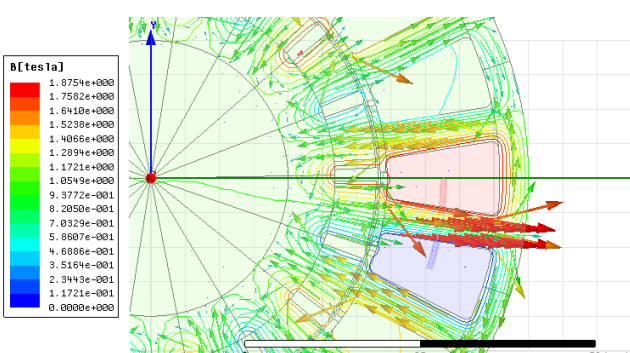


Fig. 5. Flux lines distribution with rotor axis aligned with the fed coil (feeding of phase A , static FEM analysis).

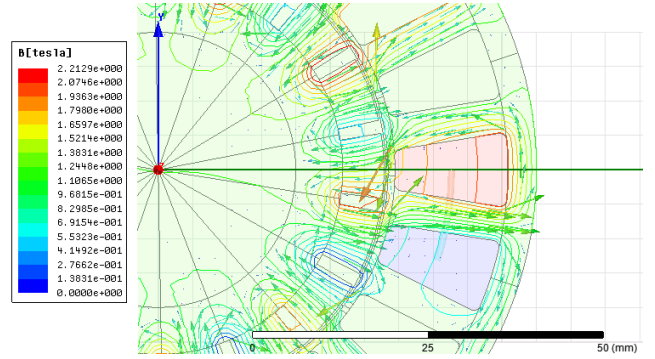


Fig. 6. Flux lines distribution with the rotor axis in quadrature with the fed coil (feeding of phase A , static FEM analysis).

B. Circuitual motor model

By assuming the magnetic independence between the phases, the voltage balance of the generic phase x of the multiphase motor can be expressed as:

$$V_x = RI_x + \frac{d\Psi_x(I_x, \theta)}{dt} \quad (1)$$

where V_x is the phase voltage, I_x is the phase current, Ψ_x is the flux linkage, R is the phase resistance, and θ is the mechanical rotor position.

The time-derivative of the flux linkage accounting for the dependence on the current and rotor position, can be written as (the subscript x is omitted for simplicity):

$$\frac{d\Psi(I, \theta)}{dt} = L_d(I, \theta) \cdot \frac{dI}{dt} + K_e(I, \theta) \cdot \omega_m \quad (2)$$

where L_d and K_e are the differential inductance and the motional voltage factor, and $\omega_m = d\theta/dt$ is the rotor mechanical speed.

By substituting (2) into (1) one has the voltage balance in the form:

$$V = RI + L_d(I, \theta) \cdot \frac{dI}{dt} + K_e(I, \theta) \cdot \omega_m \quad (3)$$

where one recognizes the inductive and the motional voltage drops, respectively given by:

$$\Delta V_{di}(I, \theta) = L_d(I, \theta) \cdot \frac{dI}{dt} \quad (4)$$

$$E(I, \theta) = K_e(I, \theta) \cdot \omega_m \quad (5)$$

Equation (3) represents the electrical dynamics of the machine: providing the motion equations to calculate the mechanical speed and position, it allows to compute the phase current according to voltage inputs and the knowledge of the functions $L_d(I, \theta)$ and $K_e(I, \theta)$.

Notice that these functions are a non-linear generalization of the self-inductance and back-EMF constant of the usual lumped parameter models of PM machines, and they can be achieved by a static FEM computation of the flux linkage because they are expressed as:

$$K_e(I, \theta) = \left. \frac{d\Psi(I, \theta)}{d\theta} \right|_I \quad (6)$$

$$L_d(I, \theta) = \left. \frac{d\Psi(I, \theta)}{dI} \right|_\theta \quad (7)$$

For the sake of its implementation in a circuital based dynamic simulator, the electrical model of the motor phase is divided into a “voltage model”:

$$\Delta V_{di} = V - RI - E(I, \theta) \quad (8)$$

and a “current model”:

$$I(t) = I(t_0) + \int_{t_0}^t \frac{\Delta V_{di}}{L_d(I, \theta)} dt \quad (9)$$

where the first is obtained by substituting the definition (4) into (3), and the second is the integral form of eq. (4).

Fig. 7 shows the circuital implementation of the voltage model by using the SimPowerSystem tool of Matlab/SimulinkTM. It includes a voltage controlled source to take into account the motional voltage term, but the key element is the current controlled source which injects the phase current. In fact, the voltage drop at the terminals of the current source is bound to satisfy both the voltage balance at phase terminals and the current model integration as a signal, this last shown in Fig. 8. The same figure shows the run-time reading of the look-up-tables storing the non-linear functions $L_d(I, \theta)$ and $K_e(I, \theta)$, computed by the FEM analysis, and the calculation of the motional voltage needed in the voltage model.

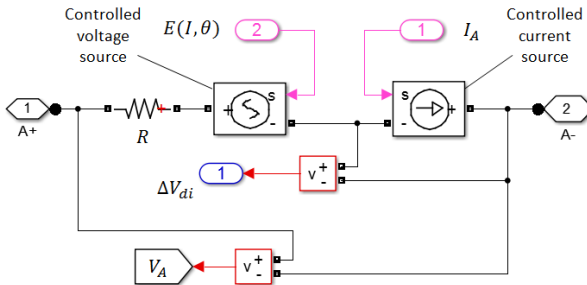


Fig. 7. Circuital model of the motor phase (voltage model).

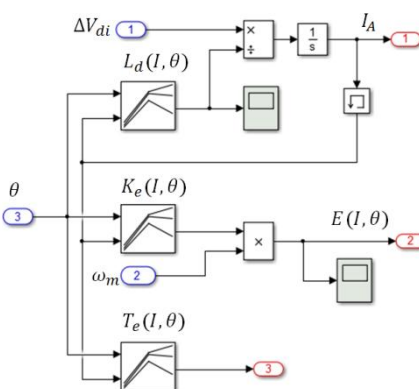


Fig. 8. Current model and reading of the model functions LUTs.

As for the electromagnetic torque, needed to provide the

input of the mechanical part of the model, the straightforward solution in off-line co-simulation approach (see Section IV) is to add the torque (besides the flux) to the output of the FEM analysis, and to use the stored torque map vs. current and position (i.e. accounting all the machine non-linearity) at run-time. This is also shown in Fig. 8.

A specific study on the torque production of the machine has been presented by the authors in [24]. Based on FEM computations, it is calculated that the overall motor torque can be computed by the sum of the contributions of each single phase with a maximum difference of about 3.4% over an extended current range (see Table III, where ΔT_e is the difference between the torque computed by single phase modeling and the actual torque).

TABLE III: MODELING ERROR IN TORQUE PRODUCTION

Motoring	ΔT_e	Braking	ΔT_e	
30 A	2,0%	30 A	2,0%	
20 A	3,1%	20 A	3,3%	
15 A	3,2%	15 A	3,4%	← worst case
10 A	1,4%	10 A	1,9%	
7 A	0,2%	7 A	0,6%	
3 A	-0,5%	3 A	-0,01%	

In summary, the implementation of the proposed model requires the following steps, Fig. 9:

1st: extensive FEM magneto-static calculations to obtain the phase flux and torque maps over the whole electric period and current range (as those shown in Fig. 3 and Fig. 4). The maps resolution must be selected to achieve the proper compromise between accuracy and computation time;

2nd: interpolation and post-processing of the flux map to obtain the model functions L_d and K_e . These functions are stored in look-up tables to be readable by the dynamic simulation tool;

3rd: dynamic computation of the circuital model (voltage and current) and torque production for each phase of the machine, by taking into account of the displacement of each stator phase to the rotor poles;

4th: dynamic computation of the mechanical model of the machine, where the overall torque is computed by summing the contributions of all the phases.

The computed model functions L_d and K_e of the PM considered in this paper are reported in Fig. 10 and Fig. 11, respectively. Their behaviors testify the high non-linearity of the machine.

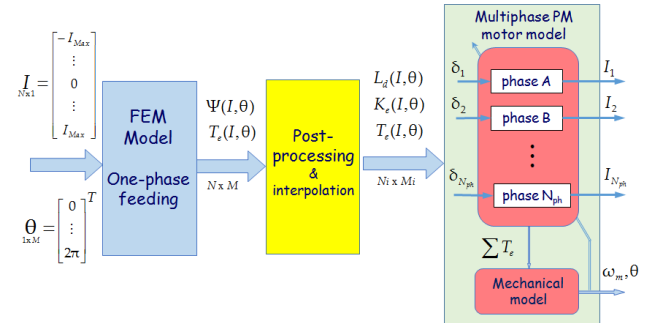


Fig. 9. Implementation steps of the fault-tolerant PM motor model.

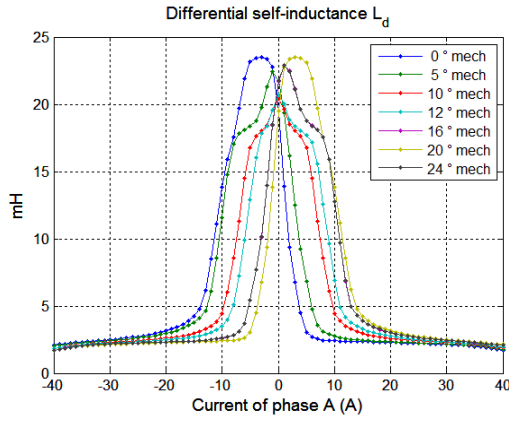


Fig. 10. Differential self-inductance L_d .

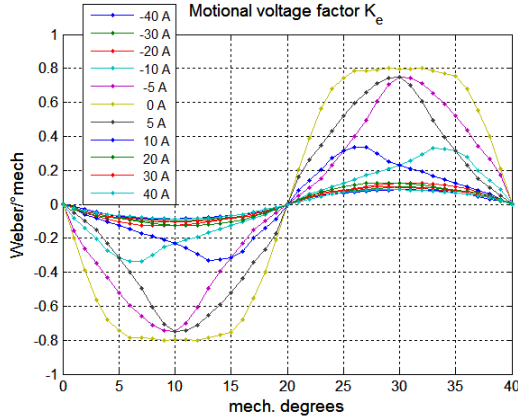


Fig. 11. Motional voltage factor K_e .

C. Mutual flux effects between phases

In the alternate teeth windings structure the maximum mutual coupling effect occurs between adjacent phases, as they share a not-wound tooth between them to close the respective flux paths.

Hence, by considering the phase-A to fix the ideas (see Fig. 2), its flux linkage is affected by the currents in the adjacent phases E and B and can be expressed as:

$$\Psi_A = \Psi_A(I_A, I_E, I_B, \theta) \quad (10)$$

so that the time-derivative gives:

$$\frac{d\Psi_A}{dt} = L_d \frac{dI_A}{dt} + M_{dE} \frac{dI_E}{dt} + M_{dB} \frac{dI_B}{dt} + K_e \omega_m \quad (11)$$

where M_d is the differential mutual-inductance between adjacent phases, and due to the symmetry of the “alternate teeth” structure one can assume:

- $L_d = L_d(I_A, I_\Sigma, \theta)$,
- $M_{dE} = M_d(I_A, I_E, \theta)$,
- $M_{dB} = M_d(I_A, I_B, \theta)$,
- $K_e = K_e(I_A, I_\Sigma, \theta)$,

with $I_\Sigma = I_E + I_B$.

These parameters have been computed by a FEM analysis to evaluate their values over an extreme operating range of currents (± 20 A) and the whole rotor position period. The

study has proven that:

- the dependence on I_Σ introduces a difference in the self-inductance L_d at maximum of 1.2% respect to the values achieved in single phase feeding (Fig. 12), while the difference in the motional voltage factor K_e is negligible;
- The mutual inductance M_d do not exceed the 2% of the self-inductance (Fig. 13 and Fig. 14).

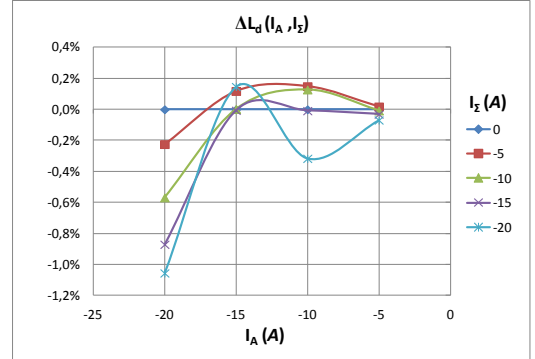


Fig. 12. Modeling error of the differential self-inductance L_d ($\theta = 10^\circ$, worst case).

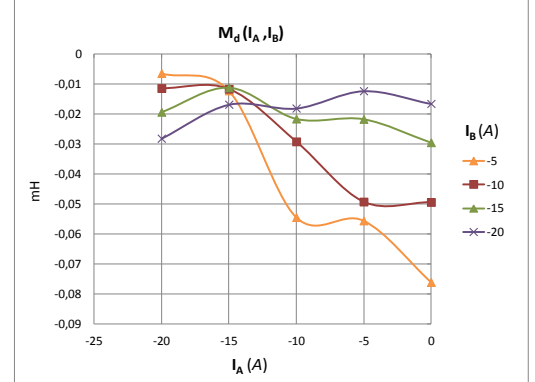


Fig. 13. Mutual self-inductance M_d ($\theta = 10^\circ$, maximum value).

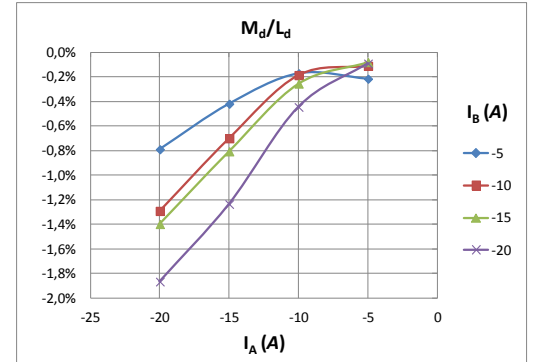


Fig. 14. Ratio between the differential mutual and self-inductance M_d and L_d ($\theta = 10^\circ$, maximum value).

Nevertheless, the mutual inductance affects the model by the product of the current time-derivative, which could be considerable in PWM operation and cannot be evaluated by static FEM analyses. For this reason, locked-rotor short-circuit tests have been done on the motor prototype as follows.

With the adjacent phase B short-circuited and the rotor

locked, current steps are imposed to the phase A, while the remaining phases are opened. In these conditions the current in the shorted phase B is driven by the only quantity:

$$-M_{dB}(I_A, I_B, \theta) \frac{dI_A}{dt} \quad (12)$$

Fig. 15 shows the test when the rotor is locked at $\theta = 10^\circ$, the position where the maximum values of M_{dB} are globally attained (see Fig. 13).



Fig. 15. Mutual coupling short-circuit test ($\theta = 10^\circ$, maximum value).

The current induced by the mutual coupling is negligible respect to the operating values. This result confirms that the alternate teeth windings structure really assure magnetic independence between the motor phases and allows for the adoption of single phase dynamic modeling for the machine.

IV. DRIVE SCHEME AND SIMULATION MODEL

The drive scheme of the fault-tolerant 5-phase PM motor is shown in Fig. 16.

The motor is designed to operate with the BLDC control technique according to the feeding strategy presented in Fig. 17.

Hall sensors are used to detect the rotor position and evaluate ten feeding sectors (S1-S10) over the electric period. Independent current control loops are implemented for each phase. Their goal is to provide, in each sector, constant current coherent in sign with the respective no-load back-EMF, while the phase where back-EMF is zero crossing is opened or its current is controlled toward zero, (4-phases-on feeding strategy).

The power converter is composed by an H-bridge inverter for each phase as represented in Fig. 18. This configuration ensures the electrical insulation needed to provide for fault tolerance. In particular when a phase is internally damaged, it can be excluded by opening the four switches of the related H-bridge. The gate signals of the power switches (d_1 to d'_2) are generated by the Proportional-Integral (PI) regulation of the phase current, arranged in per-units. The output of the current regulator represents the phase voltage command; it is the input of a PWM module which implements the bipolar modulation technique. An external PI speed control loop generates the amplitude of the references for the inner current loops. All the regulators provide output limitation and anti-windup feature.

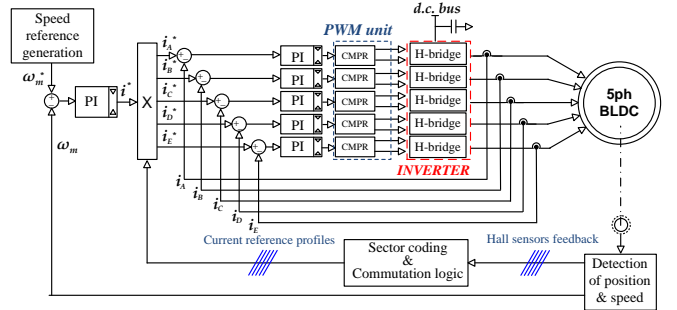


Fig. 16. Drive scheme.

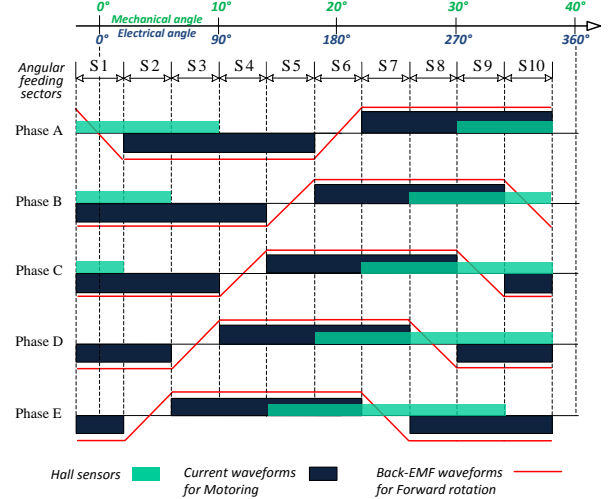


Fig. 17. BLDC control strategy of the 5-phase PM motor.

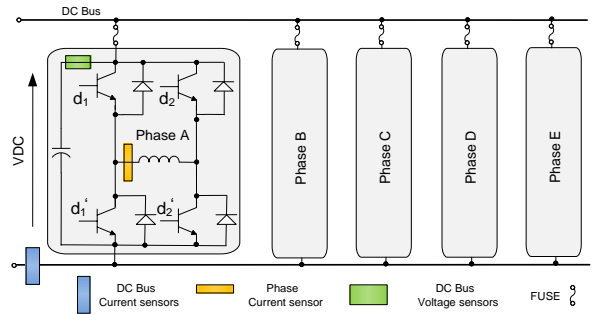


Fig. 18. Fault-tolerant power converter.

The simulation model of the fault-tolerant drive is shown in Fig. 19. Based on the single-phase modeling assumptions, it reproduces the operation of just one phase.

In the present study, speed control is omitted, to avoid interference with the internal current loop. Consequently, the speed is assumed as a constant in the mechanical model subsystem, and then the rotor position evolves linearly at runtime. The amplitude of the reference current waveform (I_{ref}) and the speed set-point ($rpmSet$) are the only inputs of the control scheme for the experimental validation presented in the next Section.

The circuit simulation scheme of the H-bridge is shown in Fig. 20. It uses discrete power components and accounts for the DC lines voltage drops and bulk capacitor. Dead-times between the upper and lower switches of the bridge legs are provided.

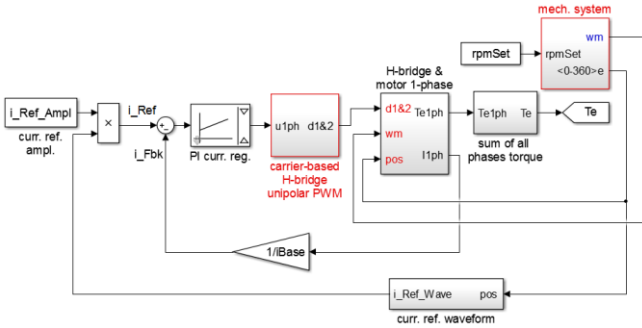


Fig. 19. Single phase simulation scheme.

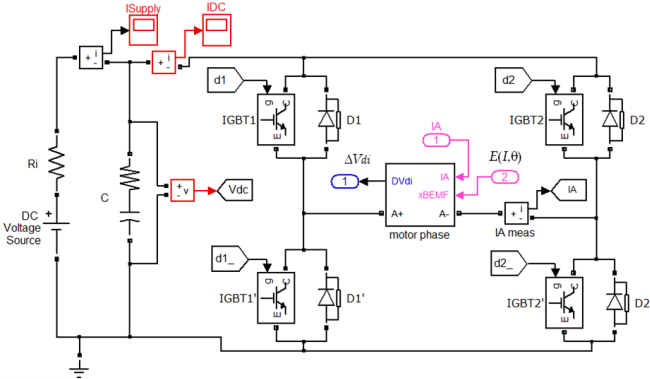


Fig. 20. Single phase H-bridge: circuitual simulation model.

V. EXPERIMENTAL VALIDATION

Fig. 21 shows the development platform used for the experimental validation of the proposed non-linear model.

The inverter features up to six independent feeding modules, each of which integrates a single phase IGBT inverter and current sensor according to the structure reported in Fig. 18, the DC bus is fed at 250 V. Power electronics is managed by a TMS320F2808 Micro-Controller Unit (MCU) that executes the control algorithm at about 15 kHz. The set-up includes a real-time debugging interface which allows for the simultaneous display of up to 4 variables processed by the control algorithm at the same control rate. To this purpose a DAC converter has been interfaced through the high speed Serial Peripheral Interface (SPI) of the MCU.

Fig. 22 shows the 5-phase PM motor for flap-actuator and the Hysteresis Brake Dynamometer MAGTROL HD-815 (rating 28 Nm, 6 kW) used for the constant load torque tests. Redundant Hall-Effect sensors and incremental encoders, embedded in the actuator, provide the feeding angular sectors and continuous position and speed signals, respectively, needed for control.

Test at different speed and load torque conditions are carried on, which required different set-up of the PI current regulators, due to the non-linear behavior of the machine. The simulation model is arranged to replicate all the relevant test conditions, namely PWM frequency, sampling time and control delays, controller's algorithms and values of the PI gains, dead-time engine of the MCU. A Runge-Kutta fixed-step solver is adopted with a step time of 0.5 us.

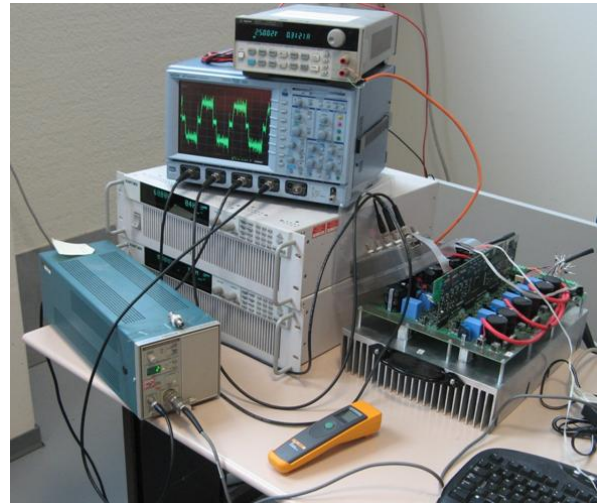


Fig. 21. Experimental set-up showing the Multiphase Drive prototype.



Fig. 22. 5-phase PM motor and loading test-bench.

Fig. 23 presents the results of a test carried out at half of the rated speed and load torque conditions. The currents of adjacent phases A and B are shown, plotted with the respective voltage commands. The PI gains of the discrete current regulators are tuned as $k_p = 1.747$ and $k_i = 0.152$, respectively.

The test is reproduced in simulation in Fig. 24. One notices the good correspondence with the experiment, both in values and shapes. Particularly, the joined correspondence of voltage and current is a proof that the overall electrical model applies.

Fig. 25 presents the results of a test carried out at one-sixth of the rated speed (low speed), and a quarter of load torque. The current of phase A and its reference are shown, plotted along with the speed signal. The PI gains of the current regulators are tuned as $k_p = 2,284$ and $k_i = 0.659$, respectively.

The related simulation is shown in Fig. 26. Also in this case one notices a good correspondence with the experiment, both in values and shapes. Most of difference is due to the noise affecting the current reference in experiment, due to the action of the speed regulator.

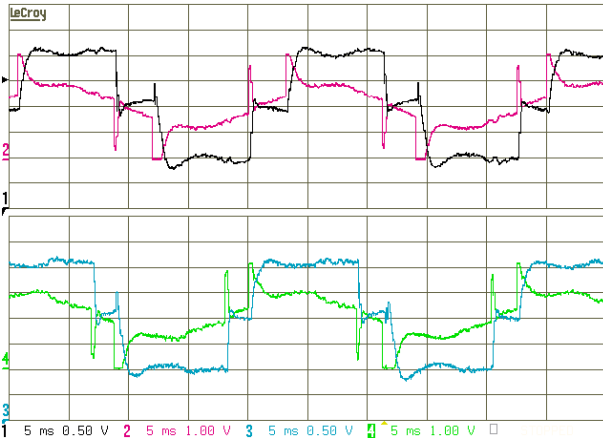


Fig. 23. Currents (1,3) and command voltages (2,4) for phases A (up) and B (down) @ 300 rpm and 6.3 Nm load torque. Scaling factors: 1 div = 1.25 A (current), 1 div = 120 V (voltage).

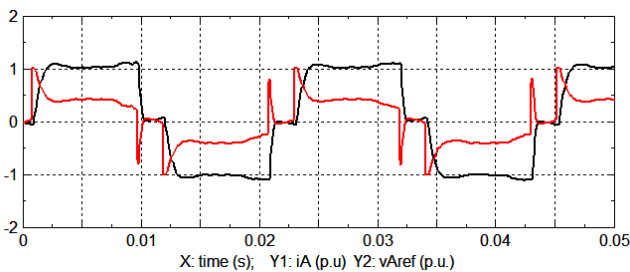


Fig. 24. Off-line co-simulation of the experiment in Fig. 23: phase current (black) and command voltage (red) @ 300 rpm and 6.3 Nm (average) torque. Scaling factors: 1 pu = 2.5 A (current), 1 pu = 240 V (voltage).

Fig. 27 presents the results of a test carried out at about rated speed (high speed) and a quarter of load torque. The current of phase A and its reference are shown, plotted along with the speed signal. The gains of the current regulators are the same of the previous (low speed) case.

The related simulation is shown in Fig. 28. The correspondence with the experiment is excellent, both in values and shapes. In fact, at high speed the noise affecting the current reference in experiment is lower due to the low-pass action of the speed regulator. By the comparison of the current waveforms in Fig. 25 and Fig. 27, it is clear how the performance of the current control deteriorate at increasing speed. In fact, the disturbance action of the back-EMF increases with the speed, for that the gains of the current loop should be adapted to maintain a good regulation.

Fig. 29 shows four of the five phase currents during a test at full load and one-half of rated speed. The PI gains of the discrete current regulators are tuned as $k_p = 2.716$ and $k_l = 0.151$, respectively, where the P action has been increased to compensate for the reduction of the differential induction at high currents.

The test is reproduced in simulation in Fig. 30. The correspondence with the experiment is good, both in values and shapes. The experiment exhibits some small oscillations triggered by the step down of an adjacent current, an effect which is not present in the simulation. This coupling effect is due to the voltage drop on the shared DC bus (see Fig. 18), more than a lack of accuracy of the motor model.

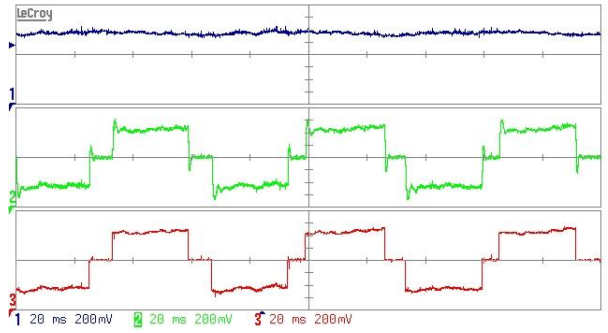


Fig. 25. Speed (1), current (2), and current reference (3) of phase A @ 100 rpm and 3 Nm load torque. Scaling factor: 1 div = 0.5 A (current).

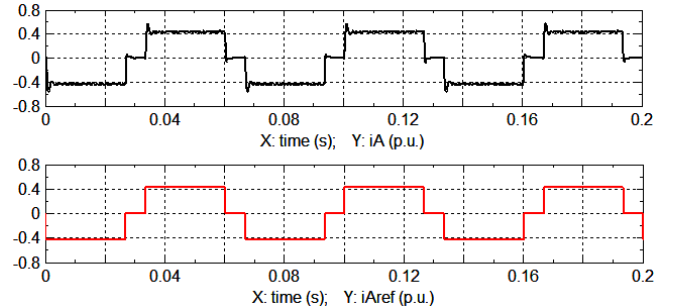


Fig. 26. Off-line co-simulation of the experiment in Fig. 25: phase current (up), and current reference (down) @ 100 rpm and 3 Nm (average) torque. Scaling factor: 1 p.u. = 0.5 A.

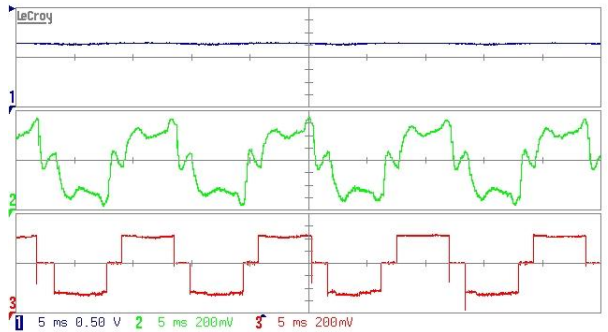


Fig. 27. Speed (1), current (2), and current reference (3) of phase A @ 575 rpm and 3 Nm load torque. Scaling factor: 1 div = 0.5 A (current).

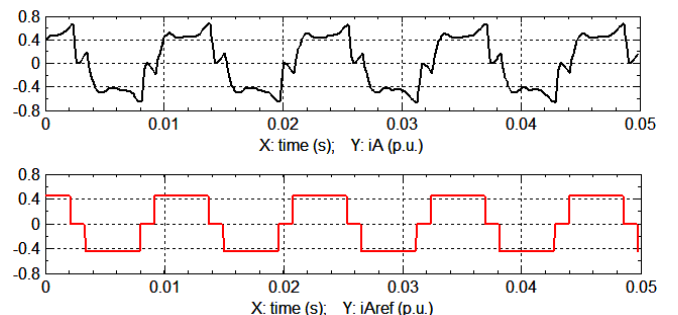


Fig. 28. Off-line co-simulation of the experiment in Fig. 27: phase current (up), and current reference (down) @ 575 rpm speed and 3 Nm (average) torque. Scaling factor: 1 p.u. = 0.5 A.

Finally, Fig. 31 refers to the same load and speed conditions the previous test but with two open phases, in order to evaluate the operation at saturating current levels. The same PI gains of the previous case are assumed.

The test is reproduced in simulation in Fig. 32. The correspondence with the experiment is excellent, both in values and shapes. It is evident the increase of the current derivative during the step-up front, which is due to the reduction of the differential inductance (and then of the electrical time-constant) at high currents.

VI. CONCLUSIONS

This paper demonstrates that the fault-tolerant PM motors with alternate teeth windings structure can be represented by the straightforward superposition of the effects of each single phase assumed to operate alone.

A non-linear model suitable for the off-line co-simulation of such kind of machines is proposed, based on a finite element analysis. It is arranged in a circuital form where the inductive parameters and back-EMF coefficient are replaced by current and rotor position dependent functions, so that the exact electromagnetic nature and geometry of the machine is accounted.

The model is validated by experiments carried on a five-phase PM motor-drive for flap applications, in different speed and load conditions, both in healthy and faulty modes. Each test is replicated by a corresponding simulation.

The results show that the modeling solution is capable to simulate the motor dynamics with a high degree of accuracy, and can be used for an effective rapid prototyping of fault-tolerant drives.

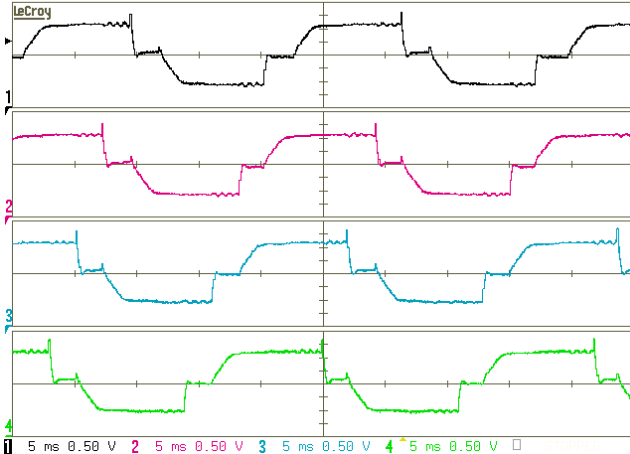


Fig. 29. Currents in phases A, B, C, and D (from up-to-down) @ 300 rpm and 12.7 Nm load torque, healthy operation. Scaling factor: 1 div = 2.5 A.

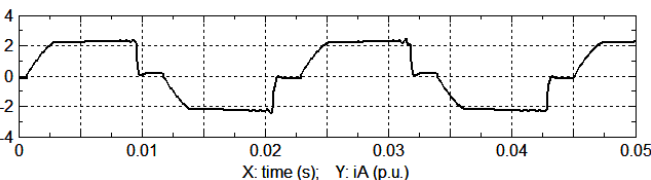


Fig. 30. Off-line co-simulation of the experiment in Fig. 29: phase current @ 300 rpm and 12.7 Nm (average) torque. Scaling factor: 1 pu = 2.5 A.

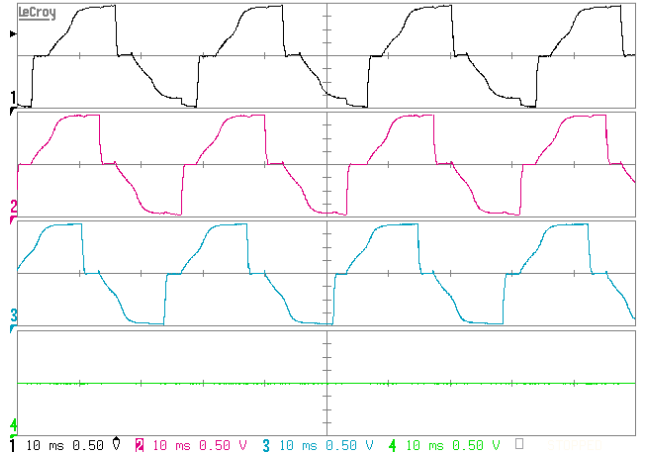


Fig. 31. Currents in phases A, B, C, and D (from up-to-down) @ 245 rpm and 12.7 Nm load torque, two open phases. Scaling factor: 1 div = 5 A.

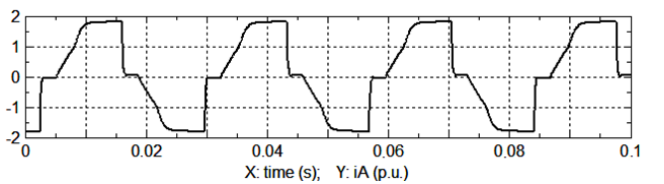


Fig. 32. Off-line co-simulation of the experiment in Fig. 31: phase current @ 245 rpm and 12.7 Nm (average) torque. Scaling factor: 1 pu = 10 A.

VII. REFERENCES

- [1] Chee-Mung Ong, "Dynamic Simulation of Electrical Machinery using Matlab/Simulink", Prentice Hall PTR, Upper Saddle River, NJ (USA), 1998.
- [2] C. D. French, J.W. Finch, P.P. Acarnley, "Rapid prototyping of a real time DSP based motor drive controller using Simulink", Proc. of Int. Conf. on Simulation, 1998, pp. 284-291.
- [3] O.A. Mohammed, S. Liu, Z. Liu, "A phase variable model of brushless dc motors based on finite element analysis and its coupling with external circuits", IEEE Trans. on Magnetics May 2005, vol. 41, pp. 1567-1579.
- [4] M. Fazil, K.R. Rajagopal, "Nonlinear Dynamic Modeling of a Single-Phase Permanent-Magnet Brushless DC Motor Using 2-D Static Finite-Element Results", IEEE Trans. on Magnetics, April 2011, vol. 47, pp. 781-786.
- [5] A. Gautam, S. Karugaba, J. Ojo, "Modeling of nine-phase interior permanent magnet machines (IPM) including harmonic effects", Proc. of IEEE Int. Electric Machines & Drives Conf. (IEMDC), 2011.
- [6] F. Parasiliti, M. Villani, A. Tassi, "Dynamic analysis of synchronous reluctance motor drives based on Simulink® and finite element model", Proc. of IECON 2006, 32nd Annual Conf. on IEEE Ind. Electronics, Paris, France, 6-10 November 2006, pp. 1516-1520.
- [7] Wenxiang Zhao, Ming Cheng, Xiaoyong Zhu, Wei Hua, Xiangxin Kong, "Analysis of Fault-Tolerant Performance of a Doubly Salient Permanent-Magnet Motor Drive Using Transient Cosimulation Method", IEEE Trans. on Industrial Electronics, 2008, Vol. 55, Issue 4, pp. 1739-1748.
- [8] G. Scelba, G. De Donato; F. Giulii Capponi; A. Consoli; O. Honorati, "A co-simulation platform for evaluation of sensorless control techniques for IPMSMs". Proc. of Int. Conf. on Electrical Machines (ICEM), Rome, 6-8 Sept. 2010, pp. 1-7.
- [9] D. Uygun, S. Solmaz, "Design and dynamic study of a 6 kW external rotor permanent magnet Brushless DC motor for electric drivetrains", Proc. of Power Engineering, Energy and Electrical Drives (POWERENG), Riga, May 2015, pp. 87-92.
- [10] M. Ruba, D. Fodorean, "Analysis of Fault-Tolerant Multiphase Power Converter for a Nine-Phase Permanent Magnet Synchronous Machine", IEEE Trans. on Industry Applications, 2012, Vol. 48, Issue 6, pp. 2092-2101.

- [11] L. Di Leonardo, F. Parasiliti, M. Tursini, M. Villani, "Transient Analysis of PM Synchronous Motor Drives by Finite Element Model co-Simulation", Proc. of IECON 2013 Conf., Vienna, Nov. 2013, pp. 6834-6840.
- [12] M. A. Jabbar, H. N. Phyu, Z. Liu, C. Bi, "Modeling and numerical simulation of a brushless permanent-magnet DC motor in dynamic conditions by time-stepping technique", IEEE Trans. on Industry Applications, May-June 2004, Vol. 40, pp. 763-770.
- [13] "MotorSolve: Electric Machine Design Software", Infolytica Corporation, <http://www.infolytica.com/>.
- [14] "AC Motor Drive Using Cosimulation", ANSYS Inc, www.ansys.com/
- [15] R. Bojoi, S. Rubino, A. Tenconi, S. Vaschetto, "Multiphase electrical machines and drives: A viable solution for energy generation and transportation electrification", Proc. of Int. Conf. and Exposition on Electrical and Power Engineering (EPE), 2016.
- [16] G. Meng, H. Xiong, H. Li, "FEM analysis and simulation of multi-phase BLDC motor", Electrical Machines and Systems (ICEMS) Tokyo Nov. 2009, pp. 1-3.
- [17] F. Barrero, M.J. Duran, "Recent Advances in the Design, Modeling, and Control of Multiphase Machines—Part I", IEEE Trans. on Industrial Electronics, 2016, Vol. 63, Issue 1, pp. 449-458.
- [18] T. Gopalarathnam, H. A. Toliyat, J. C. Moreira, "Multi-phase fault-tolerant brushless DC motor drives", Proc. of Ind. Appl. Conf., Vol. 3, pp.1683–1688, 2000.
- [19] M. Villani, M. Tursini, G. Fabri, L. Castellini, "Multi-Phase Fault Tolerant Drives for Aircraft Applications", Proc. of Electrical Systems for Aircraft, Railway and Ship Propulsion (ESARS), Bologna 2010, pp.1–6.
- [20] M. Tursini, M. Villani, A. Di Tullio, G. Fabri and F. Parasiliti, "Off-line co-Simulation of Multiphase PM Motor-Drives", Proc. of Int. Conf. on Electrical Machine (ICEM), Lausanne, Switzerland, Sept. 4-7, 2016, pp. 1138-1144.
- [21] M. Villani, M. Tursini, G. Fabri, L. Castellini, "High Reliability Permanent Magnet Brushless Motor Drive for Aircraft Application", IEEE Trans. on Industrial Electronics, 2012, Vol. 59, pp. 2073-2081.
- [22] D. Ishak, Z.Q. Zhu, D. Howe "Comparison of PM brushless motors, having either all teeth or alternate teeth wound", IEEE Trans. on Energy Conversion, 2006, Vol. 21, Issue 1, pp. 95-103.
- [23] G. Li, Z. Zhu, M. P. Foster; D. A. Stone, H. Zhan, "Modular Permanent-Magnet Machines With Alternate Teeth Having Tooth Tips", IEEE Trans. on Industrial Electronics, 2015, Vol. 62, Issue 10 pp. 6120-6130.
- [24] M. Tursini, L. Di Leonardo, A. Di Tullio, "Finite Element Analysis of Fault-Tolerant PM Motors with Independent Phases", Proc. of Advances in Magnetics (AIM), Bormio, Italy, March 14-16, 2016.